Solute Transport in Unsaturated Porous Media: Effect of Spatially-correlated Disorder

Ali Saeibehrouzi[a,b,*], Ran Holtzman[b], Petr Denissenko[a], Soroush Abolfathi[a]

[a] *School of Engineering, University of Warwick, Coventry, CV4 7AL, UK*
[b] *Centre for Fluid and Complex Systems, Coventry University, Coventry, UK*

Abstract

Solute transport in unsaturated porous media is of interest in many engineering and environmental applications. The interplay between small-scale, local forces and the porous microstructure exerts a strong control on the transport of fluids and solutes at the larger, macroscopic scales. Heterogeneity in pore geometry is intrinsic to natural material across a large range of scales. This multiscale nature, and the intricate links between two-phase flow and solute transport, remain far from well understood, by and large. Here, we use Direct Numerical Simulation (DNS) to quantify the effects of correlated heterogeneity on solute transport during drainage under an unfavorable viscosity ratio. We find that increasing spatial correlations in pore sizes increases the size of the required Representative Elementary Volume (REV). We also show that increasing the correlation length enhances solute dispersivity through its impact on the spatial distribution of low-velocity (diffusion-dominated) and high-velocity (advection-dominated) regions. Fluid saturation is shown to directly affect diffusive mass flux among high- and low-velocity zones. Another indirect effect of correlated heterogeneity on solute transport is through its control of the drainage patterns via rearrangements of mobile-immobile zones. Our findings improve quantitative understanding of solute mixing and dispersion in unsaturated conditions, highly relevant to some of our most urgent environmental problems.

Keywords: Correlated Disorder; Unsaturated Transport; Pore-scale Modeling; Dispersion; Stagnant Zones; Fluid-fluid Displacement; Direct Numerical Simulation

*Corresponding author

Graphical Abstract

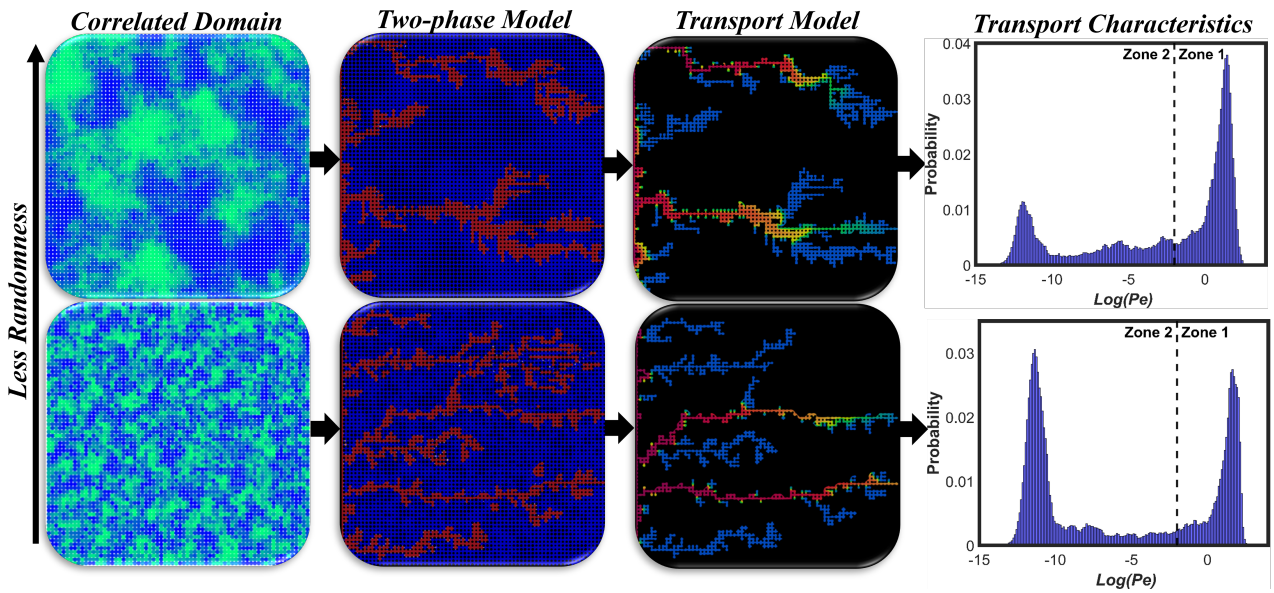

Highlights

- Solute transport in correlated media studied by Direct Numerical Simulation
- Solute dispersion increases with correlation length in pore sizes
- Quantitative analysis of the impact of correlated media requires larger domains
- Diffusive mass flux is governed by the contact boundary of mobile-immobile zones
- Lower correlation length can potentially lead to flowing-trapped zones rearrangement

1. Introduction

Transport phenomena within porous media play a pivotal role in multiple environmental and industrial processes. These applications encompass a wide range of processes, ranging from underground carbon or hydrogen storage to the migration of pollutants and contaminants in groundwater flow (Blunt, 2017). The majority of these processes occur at multiphase conditions, where two or more fluids coexist, often referred to as "unsaturated". In many cases, the fluids (e.g. gas and liquid) are immiscible, and the fluid-fluid interface serves as a boundary for solute transport, confining the tracer to a single phase only, referred to as the carrier phase therein. Mapping fluid-fluid interfaces, and the transport of solute particles in the carrier phase are the key physical processes that need to be integrated for predicting the fate of solute particles at unsaturated conditions. Depending on the application and flow condition, the percolating pathways for solute migration can be formed by either the simultaneous flow of wetting and non-wetting phase (Jimenez-Martinez et al., 2017) or the displacement of one phase by the other phase (Karadimitriou et al., 2017). In drainage (displacement of wetting fluid by non-wetting one), the focus of the current study, the spatial fluids distribution is controlled by the interplay of various forces, including viscous, capillary, gravitational, and wetting forces, in addition to the pore morphology of the media (Holtzman, 2016). The carrier phase can be categorized according to their topology into (i) interconnected regions that are reachable for the solute solution, featuring backbone/mobile and dead-end/immobile zones, and (ii) isolated regions that are unreachable for solute solution (Khayrat and Jenny, 2016). Backbone zones constitute the fully connected segments of the flow network, where the all of fluid flow takes place, while dead-end zones do not contribute to fluid flow and primarily act as a diffusion-controlled sink for tracer. In unsaturated media, solute transport is governed by the competition between advection and diffusion, which occur predominantly in the mobile and immobile regions, respectively (Karadimitriou et al., 2016). This competition is quantified by the ratio between the relative strength of advection and diffusion via the Peclet number, $P_e = \frac{uL}{D_m}$, where u is the fluid velocity, D_m denotes the molecular diffusion coefficient, and L is a characteristic length.

Both fluid flow and solute transport are directly impacted by the microstructural heterogeneity of the porous domain (Schlüter et al., 2012; Timms et al., 2018). Structural heterogeneity is an inherent feature of natural porous media, and it has been shown that macroscopic responses at large scales are governed by the distribution of solid obstacles at smaller scales (Scheibe et al., 2015; Tahmasebi and Kamrava, 2018; Armstrong et al., 2021). Unlike Darcy-scale models, pore-scale models allow for the inclusion of such small, localised properties and mechanisms by considering the domain as discrete void and solid phases (Mehmani and Balhoff, 2015). Different pore-scale modeling approaches have been developed to study pore-level mechanisms, including Pore Network Modeling (PNM), Lattice Boltzmann Modeling (LBM), and Volume of Fluid (VOF). PNM simulates fluid motion on idealized pore bodies, typically represented as cylindrical shapes, connected by constraining throats. PNM incorporates simplifications to reduce computational costs and enable simulations at larger scales, but at the expense of precise medium geometry and pore-scale mechanisms. In contrast, VOF and LBM techniques offer more accurate modeling with sub-pore resolution (i.e. control volume smaller than pores/throats), but they demand more computational resources and parallel simulation on high-performing clusters. These methods are capable of capturing pore-scale processes on exact porous structures and are often referred to as direct modeling approaches (Saeibehrouzi et al., 2024).

In many natural porous materials such as soils and rocks, the medium is characterized by spatially correlated disorder in pore sizes. Overall, few studies investigated solute transport in partially-saturated media, mostly considering random disorder without any spatial correlations (Raoof and Hassanizadeh, 2013; Karadimitriou et al., 2016; Jimenez-Martinez et al., 2017; Aziz

et al., 2018, 2019; Akai et al., 2020; Noughabi et al., 2023). Much less attention has been given to the effects of correlations on unsaturated transport. Babaei and Joekar-Niasar (2016) investigated single-phase transport considering the effects of different correlation lengths and Peclet numbers. Using PNM, Dashtian et al. (2018) evaluated the relation between throat size correlation and the rate of brine evaporation within drying porous media. Borgman et al. (2019) conducted a numerical and experimental investigation to quantify the effects of correlation length on the displacement pattern and sweep efficiency across a range of injection rates and wettability states. An et al. (2020b) employed quasi-static PNM to study solute transport and multiphase flow interactions within correlated structures. Although the above-mentioned studies tried to account for the relation between correlation length and flow or transport mechanisms at the pore level, there is still no accurate and yet efficient numerical study for evaluating unsaturated transport within correlated media. For instance, the common Mixed-Cell Method (MCM) in PNM considers perfect mixing inside pore bodies and ignores the effect of parabolic velocity profile on solute shearing (Mehmani et al., 2014; Mehmani and Tchelepi, 2017). It is also well-established that the fate of solute species in unsaturated porous media fundamentally differs from saturated conditions with unsaturated transport exhibits non-Fickian behavior and long tailing in Breakthrough Curve (BTC) (Guillon et al., 2013; Jimenez-Martinez et al., 2020; Erfani et al., 2021). Therefore, results from the single-phase transport cannot elucidate unsaturated transport. Even in unsaturated media, while it is known that dispersivity (Hammel and Roth, 1998; Sato et al., 2003; Nützmann et al., 2002; Vanderborght and Vereecken, 2007; Raoof et al., 2013; Karadimitriou et al., 2017) and mixing (Ursino et al., 2001; Kapetas et al., 2014; Jimenez-Martinez et al., 2015, 2017) behaviors are influenced by multiphase conditions, the way it affects these features is unclear and one finds contradictory findings in the literature. These ambiguities underscores the necessity of establishing a more comprehensive understanding of the underlying physical mechanisms governing transport in unsaturated porous media. Another open question is how non-Fickian characteristics depend on fluid-fluid interface locations in correlated structures. Recent studies highlighted the complex dynamics of interfaces within the pore-space, showcasing frequent shuffling of flowing pathways in certain multiphase conditions (Reynolds et al., 2017; Spurin et al., 2020, 2021). For instance, in the drainage scenario, it is demonstrated that displacement under unfavorable viscosity ratios can lead to multiple "breakups" of invading phase networks even after the breakthrough, attributed to mechanisms such as snap-off (Andrew et al., 2015; Chang et al., 2019; Wei et al., 2022). In a pore-scale modeling approach such as quasi-static PNM, which excludes viscous forces, every drainage event occurs independently and each pore body is considered as a single simulation node. The percolation theory mainly considers capillarity as a local mechanism, quantified based on the idealized geometrical shape of throats (Dashtian et al., 2018; An et al., 2020b; Wang et al., 2021). Under such circumstances, achieving a fully stabilized fluid distribution is feasible since the model needs to predict whether a pore is drained, and once a flow path is established, it remains unchanged. However, experimental and numerical evidence has shown that the assumption of percolation theory does not always hold, and the location of menisci can play a crucial role in drainage dynamics (Moebius and Or, 2012; Armstrong and Berg, 2013; Raeini et al., 2014; Andrew et al., 2015). Armstrong and Berg (2013) highlighted the non-local behavior of the drainage, with the existence of a capillary pressure difference across multiple pores. It was observed that several pores can contribute to a single pore event by providing the non-wetting phase from neighbouring throats, leading to imbibition in nearby throats (i.e. receding of interface) and possible redistribution of the invading phase. Similar results were obtained by Andrew et al. (2015) using X-ray microtomography imaging in a cm-long core. The authors observed frequent snap-offs and re-connections of the non-wetting phase fingers, which can occur near the advancing front or further away from it, challenging the traditional assumptions of percolation theory. Considering such effects during the modeling of multiphase flows can be of

utmost importance as the most common approach in evaluating transport under unsaturated conditions involves a one-way analysis of transport. This means that solute solution is injected into the domain only after stabilization (i.e. steady-state) of fluid-fluid boundaries (Karadimitriou et al., 2016; Aziz et al., 2018; Hasan et al., 2019; Jimenez-Martinez et al., 2020; Ben-Noah et al., 2023). To this date, it is still unclear how the rearrangement of fluid connectivity during steady-state multiphase conditions, especially at correlated media, can impact transport performance. Contrary to the PNM approach, DNS with control volumes smaller than a single pore enables us to investigate and evaluate such behavior.

Here, we use DNS to investigate correlated microstructural heterogeneity under unsaturated conditions. This is achieved by coupling multiphase displacement and advecting-diffusing solute solution within the invaded phase. We employ a methodology to reduce the computational costs of DNS by fabricating a mask of drainage fingering pattern at steady-state conditions for the transport modeling, allowing analysis of wider numerical cases. Our numerical modeling results indicate that the size of numerical domains needs to be tuned based on correlated heterogeneity. Simulations also show that the magnitude of dispersivity is influenced by not only the invading phase saturation but also by spatial heterogeneity with higher dispersion at higher correlation length. Analysing the transport in terms of mobile/immobile regions shows that diffusive mass flux from mobile paths to immobile zones is primarily influenced by the saturation of the invading phase and the distribution of mobile and immobile zones. We find that the coupled effect of local disorder and drainage nonlocal performance can destabilise the fluid-fluid menisci, leading to the frequent rearrangement of mobile-immobile clusters.

2. Methodology

2.1. Direct Numerical Simulation

The finite-volume numerical method is adopted to develop a DNS model using the OpenFAOM (Open Field Operation and Manipulation) framework for simulating flow and transport in porous media ($www.Openfoam.org$). Incompressible Navier-Stokes (NS) equations for conservation of mass and momentum are solved for each phase i to model multiphase flow as:

$$\nabla \cdot \mathbf{u_i} = 0 \tag{1}$$

$$\rho_i \frac{\partial \mathbf{u_i}}{\partial t} + \rho_i \nabla \cdot (\mathbf{u_i u_i}) = -\nabla P_i + \nabla \cdot \left[\mu_i \left(\nabla \mathbf{u_i} + \nabla \mathbf{u_i}^T\right)\right] + \mathbf{F_s} \tag{2}$$

where, ρ denotes density, μ is viscosity, $\mathbf{u}$ is the velocity vector, P is the fluid pressure, and F_s represents interfacial forces. The evolution of fluid-fluid interfaces in both time and space is accomplished through the VOF technique. This method utilises an indicator (also called color) function (γ) to distinguish between phases as:

$$\gamma = \begin{cases} 0 & \text{for } \Omega_1 \quad \text{(Phase 1)} \\ [0,1] & \text{for } \Gamma \quad \text{(Interface)} \\ 1 & \text{for } \Omega_2 \quad \text{(Phase 2)} \end{cases} \tag{3}$$

$$\frac{\partial \gamma}{\partial t} + \nabla \cdot (\gamma \mathbf{u}) + \nabla \cdot (\gamma(1-\gamma)\mathbf{u}_r) = 0 \tag{4}$$

where $\mathbf{u}_r$ is the relative velocity between two fluids. The third term on the left-hand side of Eq. (4) is an added heuristic term in the conventional VOF formulation, aimed at minimizing the numerical

diffusion and preventing excessive spreading of the interface over multiple cells (Rabbani et al., 2016; Larsen et al., 2019). Properties at the interface are calculated through volume weighting, such that:

$$\begin{aligned} \rho &= \gamma\rho_1 + (1-\gamma)\rho_2 \\ \mu &= \gamma\mu_1 + (1-\gamma)\mu_2 \end{aligned} \tag{5}$$

The curvature of the interface (κ) is determined by the Continuum Surface Forces (CSF) model (Brackbill et al., 1992):

$$\kappa = -\nabla \cdot \mathbf{n} = -\nabla \cdot \frac{\nabla\gamma}{|\nabla\gamma|} \tag{6}$$

where $\mathbf{n}$ is unit normal vector of the interface. According to the CSF, interfacial forces in the NS equations are determined using the following formulation:

$$\mathbf{F_s} = \sigma\kappa\nabla\gamma \tag{7}$$

where, σ is the interfacial tension between fluids. The contact angle (θ) is defined for the interface-solid moving line to satisfy the following equation:

$$\mathbf{n} = \mathbf{n_s}\cos(\theta) + \tau_\mathbf{s}\sin(\theta) \tag{8}$$

with $\mathbf{n_s}$ and $\tau_\mathbf{s}$ showing vector normal and tangent to the solid wall, respectively. Pressure and velocity values are determined by using the Pressure-Implicit with Splitting of Operators (PISO) algorithm (Issa, 1986; Moukalled et al., 2016). A relative tolerance of 10^{-8} for both velocity and pressure is considered. To improve the accuracy of all simulations, the time step (Δt) is determined such that the Courant number (Co=$\frac{U\Delta t}{\Delta x}$, where U shows the magnitude of velocity, and Δx is typical mesh size) remains below 0.5. While the VOF method has been extensively used for modeling multiphase flow in porous media (Rabbani et al., 2018; Suo et al., 2020; Yang et al., 2021; Shende et al., 2021), this study conducts verification of the developed model against micromodel experiments by Roman et al. (2020) to confirm the accuracy of the employed numerical schemes. Further details and the conditions of the numerical model validation can be found in the Supplementary Material (SM) section.

The transport of solute in porous media is modeled by solving the Advection-Diffusion Equation (ADE):

$$\frac{\partial C}{\partial t} + \nabla \cdot (\mathbf{u}\, C) - \nabla \cdot (D_m \nabla C) = 0, \tag{9}$$

where C is the species concentration and D_m is molecular diffusion. In Eq. (9), the first term refers to the temporal evolution of the solute, while the second and third terms correspond to transport through advection and diffusion, respectively. A typical molecular diffusion coefficient of $10^{-9} m^2/s$ (Cussler, 2009) is adopted for all simulation scenarios investigated in this study. The time derivative is discretized using a 1^{st} order Euler implicit scheme. The diffusive and advective terms are discretized using Gauss linear corrected (2^{nd} order) and Gauss Van Leer (2^{nd} order) schemes, respectively. The transport matrix is solved with the stabilized preconditioned bi-conjugate gradient solver with a relative tolerance of 10^{-10}.

2.2. Porous Media Geometry

In this study, the domains under investigation are square structures containing cylindrical pillars in square lattices. The size of the numerical domain is $L = 70a$, where a=60 μm is the lattice length, corresponding to the distance between the center of two adjacent pores. The cylindrical pillars have

a constant height of 20 μm, and an average radius of 20 μm with a standard deviation of 4 μm. The mean value of the throat radius is 40 μm. The spatial correlation length is generated by making a random rough surface, whose Fourier transform is characterized by a Gaussian distribution of intensities centered around zero. This is accomplished by incorporating 10^4 sinusoidal waves, with wave numbers extracted from a uniform distribution, and their amplitude, orientation, and phase chosen from random uniform distributions. The correlation length (λ) of the surface has an inverse relationship with the width of this distribution in the Fourier domain, measured in units of the lattice length. A higher λ increases the likelihood of similar-sized pillars residing adjacent to each other. More information on the creation of this type of rough surface can be found in Persson et al. (2004); Borgman et al. (2017). In this study, porous media with λ of 1 (60 μm), 3 (180 μm), and 5 (300 μm) at three different realizations (domains with different random seeds but with same statistical attributes) are generated to obtain statistically representative numerical results.

2.3. Domain Discretization and Boundary Conditions

The numerical domains are created in a two-dimensional Cartesian coordinate system utilizing the OpenFOAM $SnappyHexMesh$ utility, and by employing the porous structures in STL format. Mesh sensitivity analysis follows the method outlined in Ferrari and Lunati (2013). Ferrari's study showed that differences in results between simulations using a mesh length of $\Delta x = d/12$, where Δx denotes the typical cell size and d is mean pillar diameter, and finer mesh sizes ($d/\Delta x = 15, 24, 48$) are below 10 %. To enhance simulation precision, all numerical domains are discretized with a typical cell size of 1.68 μm, resulting in nearly 4 million cells for each realization ($d/\Delta x \simeq 24$). Constant injection rate at the inlet face is imposed, while the no-slip boundary condition is applied to the side walls of the domain and the fluid-fluid-solid contact line. To generate simulation results with various degrees of saturation, distinct injection rates are applied, quantified through dimensionless capillary number Ca=$\mu_{inv} u_{\text{inv}}/\sigma$, where inv subscript denotes the invading phase. Multiphase simulations are performed at three injection rates, Ca=10^{-4}, 10^{-5}, and 10^{-6}, for all realizations, resulting in a total of 27 cases (three realizations x three correlation lengths x three injection rates). In this study, the viscosity of invading and defending fluids is set to 10^{-3} Pa.s and 10^{-1} Pa.s, respectively. The interfacial tension between the fluids is set to 70 $\frac{mN}{m}$. Initially, the domain is fully saturated with the defending fluid, and the invading fluid, acting as the non-wetting phase, is introduced into the domain with a constant contact angle of 120°, mimicking the drainage scenario at an unfavorable viscosity ratio.

After reaching steady-state conditions, a mask, with identical mesh density to the initial multiphase model, is generated based on the fingering pattern of the invaded fluid for each realization. Solute migration is then modeled within the invaded fingers using the fabricated masks, which serve as new numerical domains. This involves establishing laminar, steady-state velocity fields within the invaded fingers by solving single-phase Stokes equations. This technique reduces the computational cost by solving the transport equation in the single-phase scenario and ensures a fixed fluid map without diffusive mass flux between the phases. For all cases, the no-slip boundary condition is applied at fluid-fluid boundaries. While simplifying the calculation, this boundary condition has a negligible effect on transport characteristics (Guédon et al., 2019; Triadis et al., 2019; Jimenez-Martinez et al., 2020). See SM for details on the boundary conditions and the mask extraction process. In our simulation, the solute concentration is dimensionless and ranges from 0 (no solute) to 1 (fully saturated with solute). Initially, the invading fingers are solute-free, and the solute is introduced into the domain from the inlet with a concentration of 1. All simulations are compiled on High-Performance Computing (HPC) clusters with 32 to 64 CPUs (depending on mesh density).

2.4. Upscaling Simulation Results

Whilst simulations are done at the pore level with data of concentration fields in cells smaller than pore throat, macroscopic properties, such as dispersion coefficients, are defined for the Representative Elementary Volume (REV) of the system. On this account, it is required to upscale simulation results to examine properties at the Darcy scale. This involves Upscaling the concentration values obtained at each time step to the macroscopic scale, allowing us to determine the BTC and overall concentration-time curves within the domain. The BTCs for each case are determined by calculating the average concentration values over the outlet cells, weighted by the flux of each cell (q_i):

$$\overline{C}_e = \frac{\sum_i^N C_i q_i}{\sum_i^N q_i} \tag{10}$$

The concentration-time evolution within the domain is estimated by averaging the concentration value in each cell, with weighting based on the volume of each cell (V_i):

$$\overline{C} = \frac{\sum_i^N C_i V_i}{\sum_i^N V_i} \tag{11}$$

2.4.1. Estimating Dispersion Coefficient

The coupled effects of diffusion at the pore-level and the recurrent divergence and convergence of flow pathways in porous structures lead to hydrodynamic dispersion. Dispersion mainly accounts for deviation of velocities in pore-scale compared to the macroscopic velocity (Neuman and Tartakovsky, 2009; Sahimi, 2012). Curve fitting of data to analytical solutions is one common methodology to determine the dispersion coefficient (Karadimitriou et al., 2016; Aziz et al., 2018; Hasan et al., 2019; Erfani et al., 2021). This study adopts the analytical solution proposed by Ogata and Banks (1961) to estimate the longitudinal dispersion coefficient in the domains. For the Dirichlet boundary condition applied in the simulation (with continuous injection of solute), the 1D analytical solution of the advection-dispersion equation for the inlet solute concentration of C_0 $[C(0,t) = C_0, t \geq 0]$ in a solute free domain $[C(x,0) = 0, x > 0]$ with a zero concentration gradient condition at the outlet can be written as (Ogata and Banks, 1961):

$$C(x,t) = \frac{1}{2} C_0 \left[\operatorname{erfc}\left(\frac{x - vt}{2\sqrt{Dt}}\right) + \mathrm{e}^{xv/D} \operatorname{erfc}\left(\frac{x + vt}{2\sqrt{Dt}}\right) \right] \tag{12}$$

where, D is longitudinal dispersion coefficient, and v is macroscopic flow velocity. This analytical solution was proposed for single-phase scenarios with Fickian behavior. However, it is well-known that immobile zones alter transport characteristics to non-Fickian (Ben-Noah et al., 2023). The computational data generated by Aziz et al. (2018) has indicated that transport in flowing regions can still be approximated as Fickian during the early stages of the process. Hence, we use the solution proposed by Ogata and Banks (1961) for mobile regions exhibiting Fickian behavior. To mitigate the effects of tailing observed in the BTCs during the fitting procedure, data up to a point where the flowing fingers are nearly fully developed (i.e. averaged concentration of 0.99) are employed. The distinction between flowing (advection-controlled) and trapped (diffusion-controlled) regions is accomplished using pore-scale velocities.

2.4.2. Mass Exchange Rate Between Flowing and Stagnant Zones

Mixing is a key parameter for determining transport characteristics in porous media, especially in the presence of chemical reactions. It plays a crucial role in facilitating encounters between solute

particles already present in the domain and those introduced into the domain, aiming to homogenize concentration values in space (Borgman et al., 2023). In unsaturated media, the diffusive mass exchange between flowing and trapped regions is a significant factor in characterizing the mixing, directing solute particles from flowing networks to stagnant zones (Karadimitriou et al., 2016; Jimenez-Martinez et al., 2017). In this study, the non-Fickian Mobile-Immobile Model (MIM) is employed to analyze the DNS simulation results. The MIM estimates the mass flux between flowing and stagnant zones by employing a non-equilibrium mass transfer model (Van Genuchten and Wierenga, 1976):

$$S_{\mathrm{s}}\varphi\frac{\partial C_{\mathrm{s}}}{\partial t} = \alpha\left(C_{\mathrm{f}} - C_{\mathrm{s}}\right) \tag{13}$$

where, S_s is stagnant saturation, φ denotes porosity, C_s and C_f refer to macroscopic concentration in stagnant and flowing regions, respectively, and α is the mass transfer rate.

3. Results and Discussion

3.1. Correlated Disorder Increases the Representative Elementary Volume Size

Fluid invasion patterns, and hence the required size of REV and the domain, are sensitive to pore-scale heterogeneity, including both random and spatially-correlated disorder (Holtzman, 2016; Borgman et al., 2017, 2019; An et al., 2020b). Macroscopic models, from the fundamental conservation laws such as the advection-dispersion equation to the empirical constitutive relations such as Brooks-Corey relative permeability correlations, are computed assuming that domain size is much larger than the REV. This assumption requires the input variables to be spatially and temporally independent (Neuman and Tartakovsky, 2009; Mehmani et al., 2020). A common approach for finding the REV of a medium is determining Darcy-scale properties, e.g. porosity, at various fields of view (Erfani et al., 2021). However, in this study, the extensive number of cases, including different realizations for each λ, inhibits the implementation of such a technique.

To ensure the independence of simulations from specific realizations, the calculated macroscopic properties across all realizations are compared. Fig. 1 shows the BTCs and the corresponding dispersion coefficients, obtained using Eq. 12, for all realizations under saturated conditions at macroscopic $\overline{Pe} = \frac{U_{inlet} * L}{D_m} = 280$ with L being the length of domain. The accuracy of fitted dispersion coefficients can be evaluated by calculating the Normalized Mean Square Error (NMSE) between the fitted and numerical results as NMSE $= \|X_i - \hat{X}_i\|^2 \;/\; \|(X_i - \bar{X}_i)\|^2$, where $\|^2$ shows the 2-norm of a vector, and $\hat{X}_i$, X_i, and $\bar{X}_i$ are curve fitting output values, curve fitting input values from simulation, and mean values, respectively. In all fitting cases, the NMSE value was below 0.01. As can be seen from the figure, similar dispersion coefficients are estimated for $\lambda = 1$ and $\lambda = 3$ with superimposed BTCs. However, for the most correlated structures, the dispersion coefficient's value varies markedly from one case to another and is realization-dependent. Another evidence is provided by comparing the saturation values at the steady-state condition for all realizations across the range of applied Ca (see Fig. S5 in SM). Contrary to λ=5 with scatter values, the saturation remains nearly the same for all realizations of λ=1 and λ=3 at each injection rate. This shows that the structural heterogeneity of media with λ=5 results in a REV larger than the dimensions of the domains, making the results realization-dependent.

For the model investigated in this study, the domain size should be at least 23 times the correlation length (considering the domain size as 4.2 mm and correlation length of λ=3 or 180 μm) to obtain quantitatively representative porous media. This is aligned with the findings of An et al. (2020b). This is particularly relevant as a common approach to measure flow and transport characteristics is using images captured from X-ray microtomography, with specimens often on the

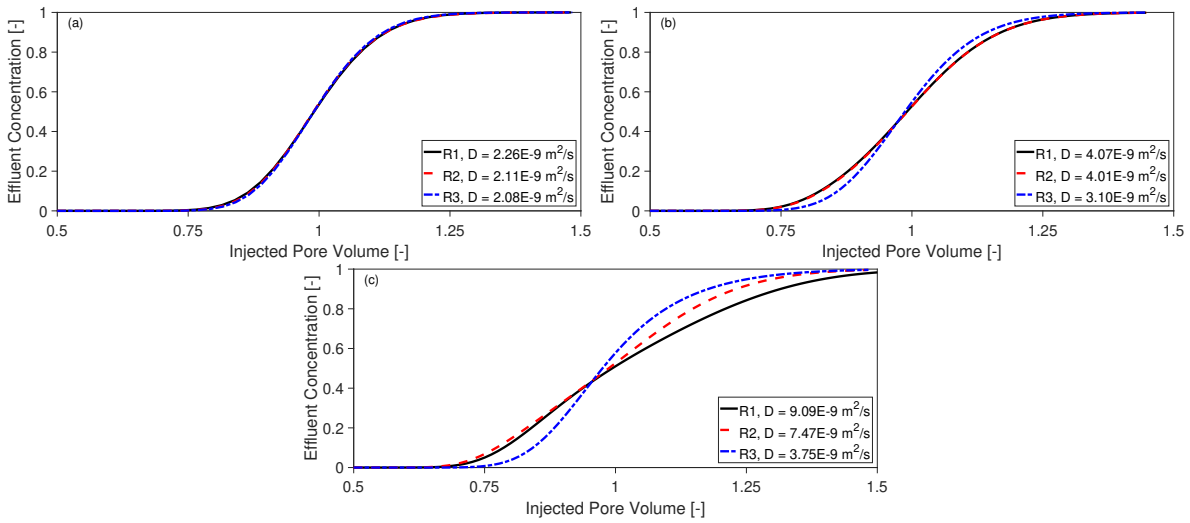

Figure 1: Breakthrough curves for three realizations (R denotes realization) simulating saturated transport at $\overline{Pe} = 280$ with fitted dispersion coefficients (D), for mediums of three correlation lengths, λ: 1, 3, and 5 in panels (a–c) respectively.

order of mm, depending on the device specifications (Moreno-Atanasio et al., 2010; Scanziani et al., 2017). In carbonate rocks, for instance, characterized by multiscale heterogeneity and correlation length in the range of >> 1 mm (Vik et al., 2013a,b), utilizing samples smaller than the REV can lead to misinterpretations. In such cases, a marginal shift in sample volume can result in substantial changes in determined bulk properties (Nordahl and Ringrose, 2008). Given these considerations and due to the runtime costs of rerunning all simulation cases with larger domain sizes, the transport analysis is focused on domains with λ of 1 and 3.

3.2. Fluid-Fluid Displacement Topology and Diffusion-Controlled Zones

The final fingering patterns across the range of applied Ca are illustrated in Fig. 2 for one set of realizations. For the lowest injection rates (Ca of 10^{-6} and 10^{-5}), the flow is predominantly governed by capillary forces. The invading phase enters throats and follows pore bodies with the path of least resistance, with branching in the transversal direction. An increase in the injection rate intensifies viscous forces, resulting in the emergence of additional pathways (fingers) for the invading phase. At a higher injection rate ($Ca = 10^{-4}$), the developed fingers stretch out primarily in the direction of flow and less perpendicular to it, resulting in thinner fingers. The coupled effect of capillary with pore morphology causes some fingers to advance obliquely and not straight, reaching the outlet diagonally (e.g. observe the formed diagonal fingers in λ=3 and 5). The displacement pattern at this injection rate ($Ca = 10^{-4}$) can be ascribed to a transitional zone between capillary and viscous fingering. This is also in agreement with previous experimental and numerical findings (Zhang et al., 2011; Wei et al., 2022).

At an identical Ca, the variation in λ significantly influences the injection phase saturation and the number of formed fingers. Higher values of λ introduce spatial heterogeneity that results in the formation of clusters of regions with similar pore radii. These clusters develop zonal contrasts in medium permeability, characterized by pathways with high fluid conductivity coexisting with pathways of low conductivity. This spatial heterogeneity not only reduces the number of formed fingers but also leads to the development of thicker fingers with larger branches in the lateral direction (e.g. compare patterns for λ=1 and λ=3 at $Ca = 10^{-5}$). According to the pore-scale $Pe{=}\frac{u*\bar{R}}{D_m}$ with $\bar{R}$ being average pillar radius (Aziz et al., 2018), the interconnected fingers of the

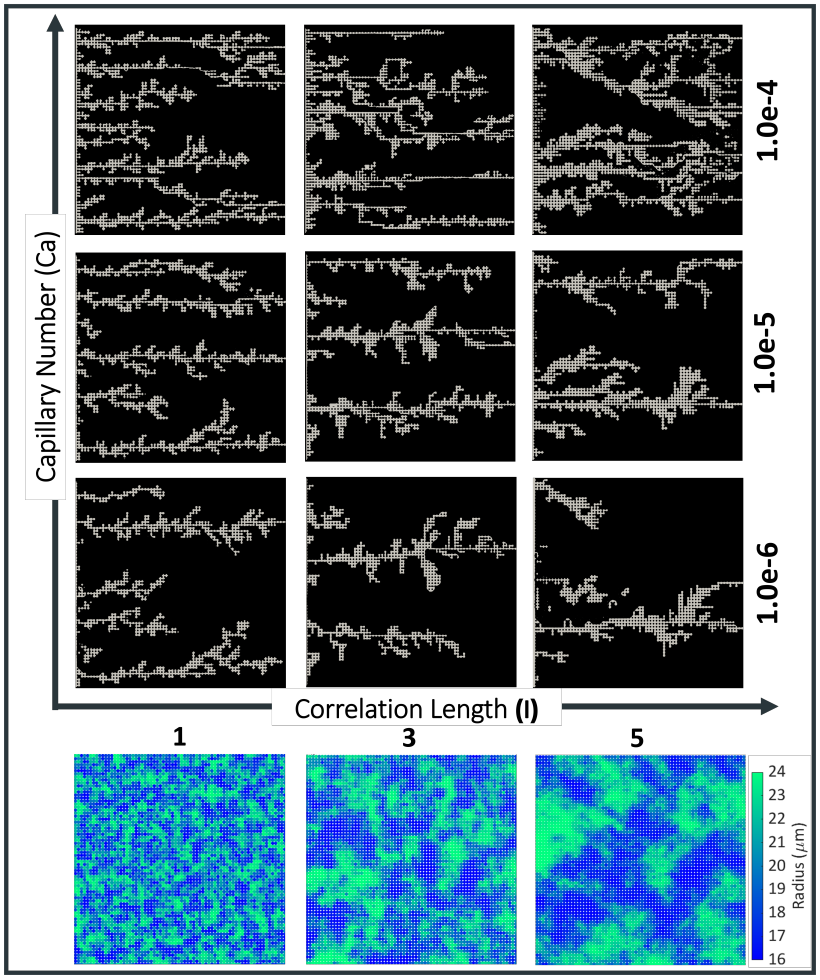

Figure 2: Two-phase fluid displacement patterns at different correlation lengths (λ) and flow rates (Ca). Flow is from left to right. White represents invading fluid, black is defending fluid and solid matrix. Bottom panels show the corresponding pillar radius distribution in one set of realizations.

invading phase can be decomposed into two parts: i) zones mostly in the direction of flow with very high velocity and dominated by advection, and ii) dead-end zones, mainly perpendicular to the mainstream of flow with remarkably small pore-scale Pe and governed primarily by diffusivity. Here, we consider the pore-scale value of Pe=0.01 as a threshold to distinguish between diffusion- and advection-controlled zones, as suggested by Babaei and Joekar-Niasar (2016). The influence of λ on the volume of diffusion-dominated zones of the invading phase network can become evident by comparing the value of trapped saturation at different degrees of invading phase saturation, S_i (displayed in Fig. 3). Trapped saturation is defined as $S_{Tr} = V_{Tr}/V_P$, with V_{Tr} denoting the total volume of trapped zones (i.e. zones of invading fingers with pore-scale $Pe \prec 0.01$) and V_P is the total pore volume of the medium. To provide a comprehensive analysis and expand the dataset range, two additional drainage simulations are conducted for realizations with λ equal to 1 and 3 at Ca of 10^{-3}, resulting in higher S_i. In Fig. 3, each S_i value corresponds to one Ca ranging from 10^{-3} to 10^{-6}.

A monotonic decrease in trapped saturation is observed for λ=1 and 3 versus S_i (Fig. 3). The results also highlight that increasing λ corresponds to a reduction in the volume of diffusion-governed zones across all S_i. This is attributed to the lack of favourable pathways at lower λ values, characterized by higher randomness in the local conductivity. At the same Ca (injection rate in our case), the lack of favourable pathways for domains with lower correlation length results in the formation of more fingers that remain trapped, i.e. do not reach the outlet, and hence are reachable for the solute solution mainly by diffusivity due to small values of pore-scale Pe.

The nonlinear relationship observed in Fig. 3 between injection rates and S_i, i.e. an order of magnitude reduction in Ca leading to a distinct reduction in S_i, can be explained by the dynamics of the drainage process. In drainage, local pore morphology predominantly influences the displacement pattern and, consequently, saturation. In accordance with the Young-Laplace equation (Young, 1805), when a non-wetting phase enters a saturated domain, the local potential energy of the non-wetting phase accumulates until it surpasses the capillary entry pressure of the widest throat, and then draining the connected pore body (Moura et al., 2020). Based on the applied pressure and pore space characterization, i.e. throats geometry and distribution, only a subset of throats are available for the penetrated phase at each Ca. Consequently, the variation in accessible pore bodies versus injection rate can exhibit a nonlinear relationship, leading to distinct S_i value (An et al., 2020a).

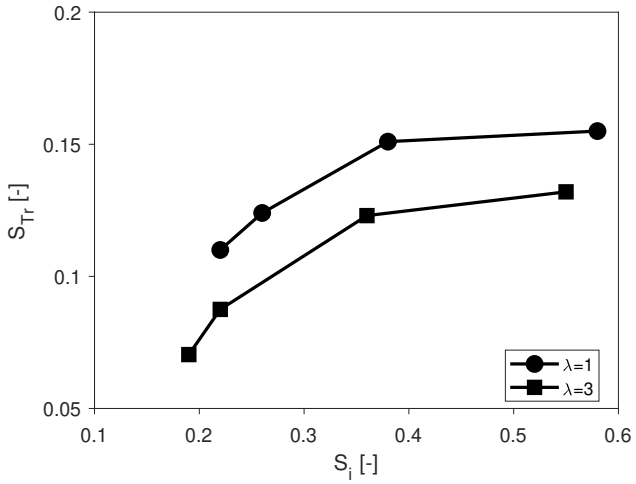

Figure 3: Variation of trapped saturation (within the invading phase) calculated at $\overline{Pe}$=280 versus invading phase saturation S_i (corresponding to Ca=10^{-3} to 10^{-6}) for different correlation lengths.

3.3. Contribution of Mobile and Immobile Zones to Transport

The fluid-fluid boundaries segment the penetrated phase network into mobile and immobile regions with distinct transport characteristics. To evaluate the contribution of each zone to the transport process, the probability of pore-level Pe at different invading phase saturation for $\lambda = 1$ are compared in Fig. 4. In the saturated case, a single peak is evident, predicting the dominance of advection in regions predominantly characterized by $Pe > 0.01$. For the unsaturated cases, two zones with a bimodal variation can be observed across all saturation ranges, demonstrating the migration of solute solution with significant contributions from both advective and diffusive forces. Zone 1 corresponds to regions with high-velocity values, where advection is the primary transport mechanism, i.e. mobile zone. The formation of dead-end branches leads to a second peak (Zone 2), characterized by low-velocity values and governed by diffusive forces. As the influence of diffusive forces intensifies, the transition from Zone 1 to Zone 2 results in the emergence of regions with an interplay of both forces (intermediate Pe), followed by regions where advection plays a minimal role (i.e. considerably small Pe).

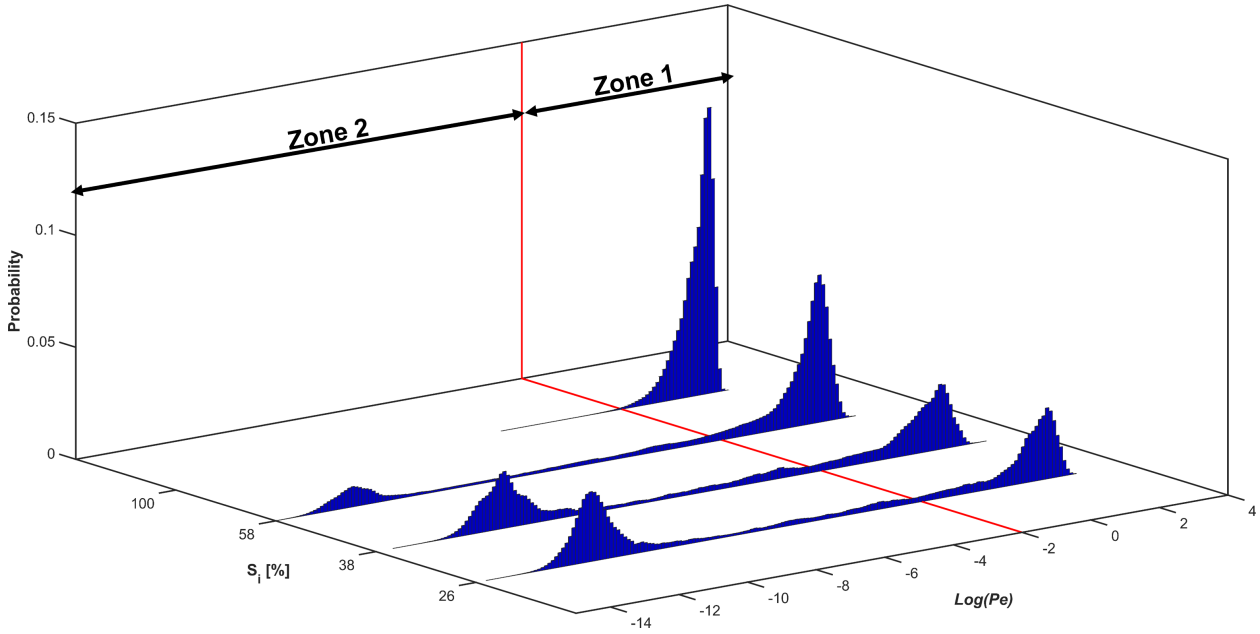

Figure 4: Probability distribution of logarithmic pore-level Pe number for $\lambda = 1$ at variable invading phase saturation S_i (corresponding to Ca=10^{-3} to 10^{-5} for $S_i \prec 100$ %). Zone 1 and 2 refer to the advective- and diffusive-dominated zones, respectively.

A notable difference among unsaturated cases is the magnitude of each peak. Comparing the overall distribution of pore-scale Pe probabilities shows that an inverse relationship exists between the S_i and the prevalence of completely diffusion-dominate zones (the peak in Zone 2) within the medium. For instance, for invading phase saturation $S_i = 26\%$, the probability of both peaks in the pore-scale Peclet number distribution is similar, indicating a nearly balanced contribution from both advection and diffusion to the transport process. At higher saturation levels (e.g. S_i=58%) the peak in Zone 2 is smaller than the corresponding peak in Zone 1. While according to Fig. 3, reducing S_i decreases the overall volume of immobile zones (Zone 2), Fig. 4 shows that at lower S_i Zone 2 is constituted mostly by totally diffusion-dominated regions with very small Pe. Multiphase pore-scale mechanisms control this behavior. At a high Ca like 10^{-3} (resulting in S_i =58%), the displacement pattern exhibits viscous fingering, facilitating the flow of the non-wetting phase predominantly in the direction parallel to the applied pressure drop. As a result, fewer dead-end

fingers, corresponding to the peak in Zone 2, are formed in both lateral and parallel directions. However, at lower injection rates multiple fully trapped fingers can develop in the direction of flow without reaching the outlet, resulting in an increase in the probability of considerably small pore-scale Pe (e.g. compare mobile and immobile zones in Fig. 5 for saturation of 58% and 22%).

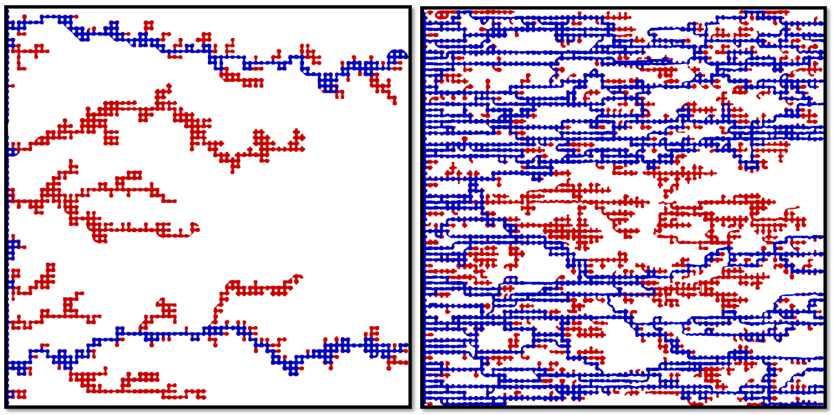

Figure 5: Comparison between mobile (blue) and immobile (red) areas in $\overline{Pe}$=280 for λ=1 at invading saturation of Left) 22% (Ca=10^{-6}), and Right) 58% (Ca=10^{-3}), in the carrier (invading) phase containing solutes. White refers to the solid and defending phase (where there is no solute transport).

3.4. Solute concentrations

Next, we show the impact of fluid velocities in solute transport under partially-saturated conditions. As predicted above from the Pe distributions, solute concentration in immobile zones increases more rapidly (with injected volumes) for higher S_i, see Fig. 6.

The cumulative volume of injected solute solution required to raise concentration in the immobile zones also increases with the macroscopic (sample-averaged) Peclet value, e.g. compare $\overline{Pe}$ of 280 with 28 in Fig. 6. This is due to the relatively low diffusivity in the domain: the weak advective forces in the immobile zones make diffusion the primary transport mechanism. Provided that solute solution is present in the mobile zones (i.e. $\overline{Pe} \gg 1$), diffusivity requires a similar amount of time to direct solute solution from mobile pathways to the immobile zones at both $\overline{Pe}$ levels for each saturation degree. This indicates that at higher $\overline{Pe}$, a large number of introduced solute solution exit the domain without being diverted toward the trapped zones. Increasing the $\overline{Pe}$ by injecting at higher rates primarily boosts advective forces in the mobile zones without any appreciable effect on transport in immobile zones. The long time required to achieve 100 % concentration in immobile zones contributes to the dual characteristic time scales of non-Fickian transport, including an early breakthrough of the solute solution with the rapid development of mobile zones (marked with red circles in Fig. 6 for the concentration of 90%), followed by a prolonged period of slow mass transfer between mobile and immobile regions. In Section 3.6 we analyze the mass flux between these zones.

3.5. Dispersion-Saturation Relation

It is widely acknowledged that transitioning from single-phase to multiphase transport scenarios can amplify tracer dispersivity by order of magnitudes, due to the constriction of available pathways for solute solution migration. However, there is no clear agreement regarding the behavior of dispersivity in unsaturated media. For instance, some studies have reported an increase in solute solution spreading with decreasing saturation (Nützmann et al., 2002; Sato et al., 2003), whereas others demonstrated a reduction in dispersion coefficients (Hammel and Roth, 1998; Vanderborght

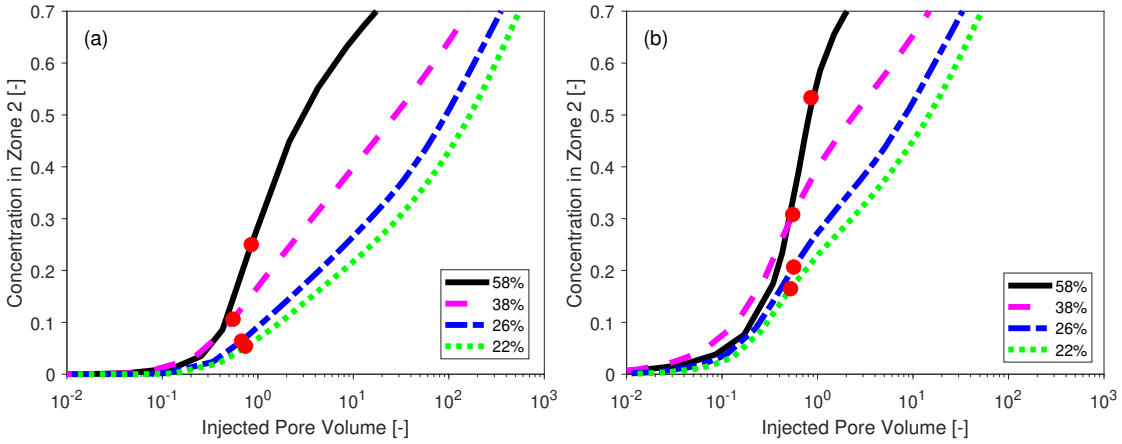

Figure 6: Solute concentrations in immobile zones (Zone 2) versus injected pore volume at a range of saturation for λ=1. a) $\overline{Pe}$=280, and b) $\overline{Pe}$=28. Red circles mark the time at which mobile zones are at 90% concentration.

and Vereecken, 2007). Some studies also presented a non-monotonic trend between dispersion coefficients and carrier phase saturation (Raoof et al., 2013; Karadimitriou et al., 2017; Zhuang et al., 2021).

To improve understanding of the equivocal nature of the dispersion-saturation relation, we compute the dispersion coefficient at various invading phase saturation for different media (spatial correlations, λ, of 1 and 3) and macroscopic Peclet values (Fig. 7). We find that increasing λ enhances the solute spreading, regardless of the value of $\overline{Pe}$ (injection rate). This can be explained by the reduced number of developed fingers at higher λ. At the same applied injection rate, a lower number of formed fingers results in a faster spreading of the entered solute solution and a shorter period of time for it to leave the domain. The non-monotonic dependence of dispersion on S_i (Fig. 7) can be attributed to the tortuosity of velocity streamlines, with the maximum dispersivity at a fluid configuration with the most heterogeneous pathways (Gong and Piri, 2020). The simulation results show that the dispersion coefficient peaks at invading phase saturation of S_i ~37 %, which belongs to the transient regime between capillary fingering and viscous fingering. The formed diagonal fingers at the transient regime increase the path length, tortuosity, for the solute solution and finally lead to an enhancement of the dispersion coefficient. At identical saturation, increasing the macroscopic $\overline{Pe}$ from 28 to 280 enhances the advective force and helps the solute solution to travel faster in flowing areas, manifesting itself by a higher dispersion coefficient.

3.6. Mobile-Immobile Mass Flux

The common perspective on mixing under unsaturated conditions suggests that concentrating the transport process into a limited number of pathways restricts mixing by reducing the residence time for tracer particles (i.e. shorter mixing time) (Kapetas et al., 2014). However, Jimenez-Martinez et al. (2015) demonstrated experimentally that fingering in the longitudinal direction can also lead to a concentration gradient in the transverse direction, enhancing mixing by promoting diffusive flux to immobile zones. Findings from multiple physical and computational studies have outlined the time-dependency of mass exchange rates between mobile and immobile parts of domain (Karadimitriou et al., 2016; Aziz et al., 2018; Hasan et al., 2019; Li and Berkowitz, 2019; An et al., 2020b). However, the variation of the mass exchange rate over time was inconsistent in the literature. For instance, Aziz et al. (2018) demonstrated a non-monotonic trend for the mass exchange rate coefficient in an uncorrelated medium, concluding two stages for mixing, including

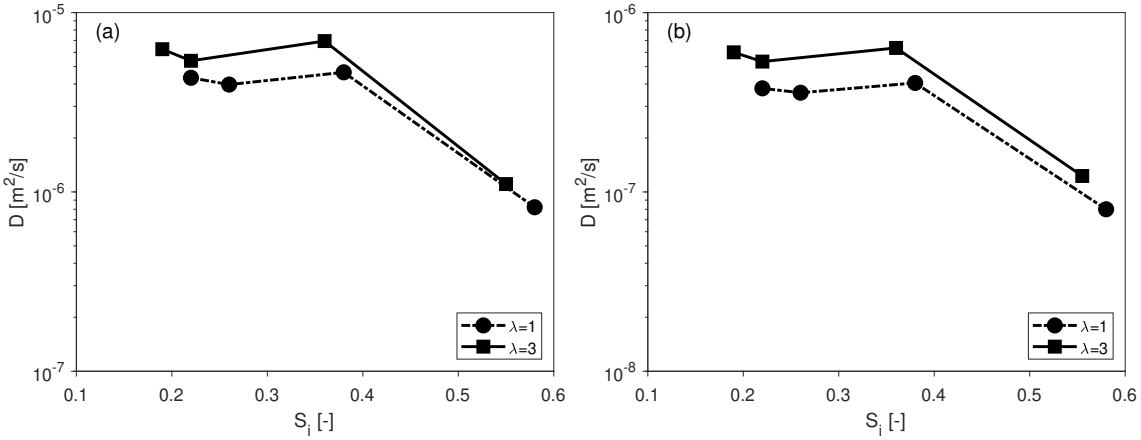

Figure 7: Dispersion-invading phase saturation relation for λ=1 and λ=3 at (a) $\overline{Pe}$=280 and (b)$\overline{Pe}$=28.

an initial increase in the mass exchange rate followed by a subsequent decrease. However, An et al. (2020b) showed a monotonic reduction in the mass transfer rate over time for both correlated and uncorrelated structures.

Fig. 8 depicts the temporal variation of mass transfer rate (α in Eq. 13) for λ=1 and λ=3 at two $\overline{Pe}$. A non-monotonic trend can be observed for $\overline{Pe}$=280 at both λ values. In the early stages of the process, the boundary area between mobile and immobile zones is established, and solute start transporting into the trapped zones, leading to the enhancement of diffusive mass flux. Due to the rapid development of mobile zones, the duration of this stage is relatively short. This stage is followed by a gradual decrease in diffusive mass flux as the tracer is directed to significantly low-velocity zones far from the mobile pathways. However, for the highest saturation at both correlation lengths, the mass exchange rate displays a monotonic decrease. The initial delay in increasing the concentration of the mobile zones, which is related to the larger clusters of flowing regions at the highest saturation, postpones the formation of the boundary area between mobile and immobile zones. Subsequently, this delay masks the initial increase of α at the beginning of the process. Similarly, for Pe=28, the mass exchange rate shows a continuous decrease for both correlation lengths at all degrees of saturation. Here, the delay in the development of mobile zones, caused by a reduction in advective forces within the domain, is responsible for masking the initial increase of α. These results clearly underline the significance of fingering topology, affecting the contact areas between mobile and immobile zones, and the ratio of advective to diffusive forces in determining the mass exchange rate. For instance, compare the difference in the magnitude of diffusive mass flux for λ=3 at the saturation of 55% with lower degrees of saturation. The temporal evolution of the mass exchange rate can vary depending on the spatial distribution of mobile and immobile clusters, and the injection rates for each fluid configuration.

3.7. Effect of Drainage Non-local Dynamics on Transport

In porous media, fluid-fluid interfaces advance through pore-scale mechanisms, such as Haines jumps and cooperative pore-filling. The prevalence of these mechanisms depends on the wettability and the rates (Ca) (Holtzman and Segre, 2015). During drainage, the pressure of the invading phase increases until it reaches the threshold required to overcome the local capillary pressure of a constriction (throat). The interface then "jumps" to the next equilibrium state within the pore body. The sequence of such events leads to fluctuations in the pressure drop along the domain, as depicted in Fig. 9, for different λ at two injection rates. A similar pressure fluctuations was observed in the drying of correlated media (Biswas et al., 2018), and forced drainage in uncorrelated media

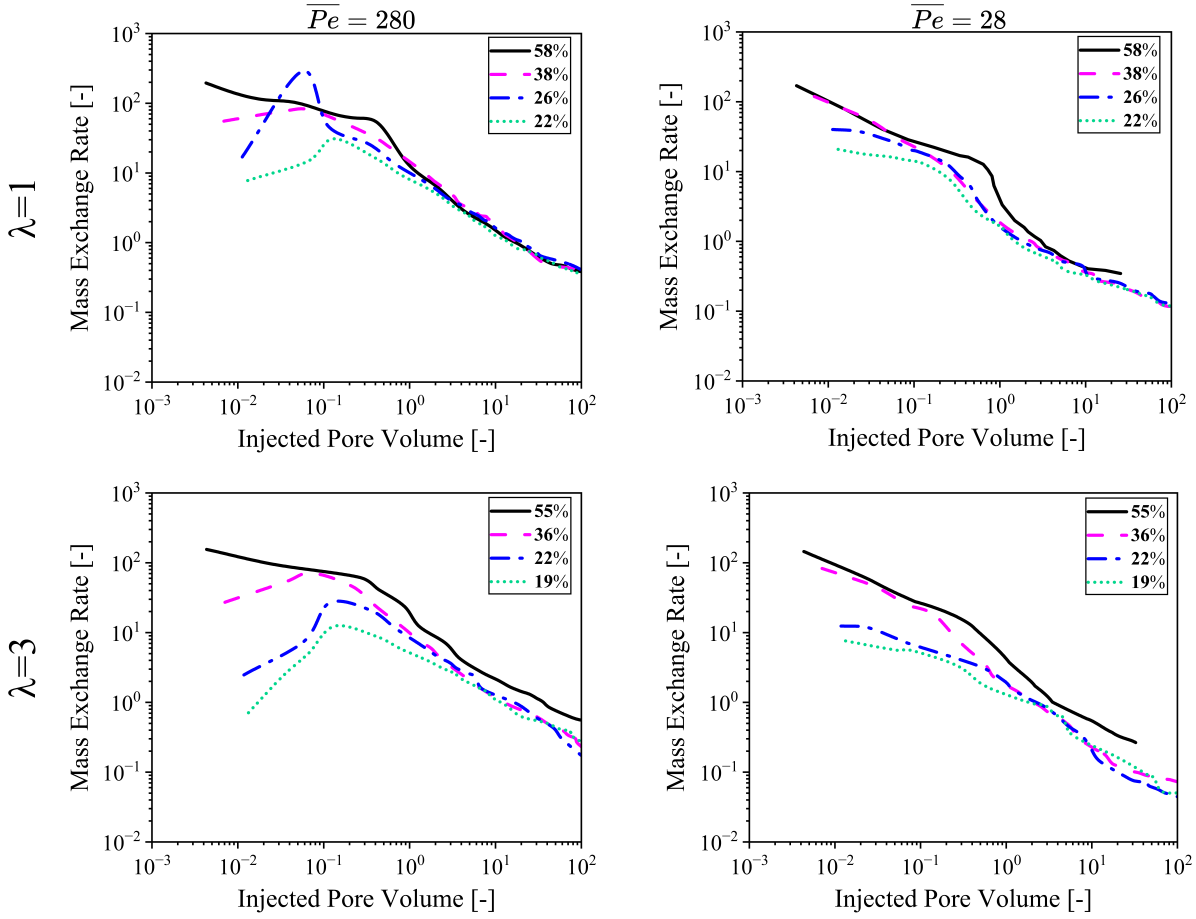

Figure 8: Temporal evolution of mass exchange rate between mobile and immobile zones for top) λ=1 and bottom) λ=3 at left) $\overline{Pe}$=280, and right)$\overline{Pe}$=28. Mass exchange rate is non-dimensionalized by $\frac{\alpha * W^2}{D_m}$ where W is the width of domain.

(Ambekar et al., 2021a,b). In all cases, the inlet pressure increases with some oscillations until the first breakthrough, which is followed by a reduction in pressure.

Fig. 9 highlights varying post-breakthrough pressure behavior across different λ values tested in this study at identical periods. In the most correlated medium, λ=5, the pressure nearly stabilizes with a small reduction after all fingers breakthrough, indicating unchanged fluid-fluid boundaries. However, pressure fluctuations persist for lower correlation lengths, particularly for λ=1. The oscillation in the pressure gradient during the post-breakthrough phase is indicative of variation in the invading phase topology. The intensity of fluctuations depends on the applied Ca. For instance, while post-breakthrough oscillation is not persistent for $\lambda = 3$ at Ca=10^{-6}, the opposite can be seen at Ca=10^{-5} with pressure fluctuation after breakthrough.

To better understand this, Fig. 10 displays the occurrence of a snap-off event within an already established finger in a domain with λ=1. As depicted in the figure, the propagation in one finger (shown with yellow) leads to interface receding in the other finger (shown with black). Recruiting some parts of the non-wetting phase for pore-level drainage events in one finger from another finger can reduce the capillary pressure far from the invasion front, and potentially destabilize the interface in the "source" finger. The destabilization of the interface continues until the pressure reaches the snap-off threshold, and the swelled wetting phase rapidly fills the throat, disconnecting parts of the

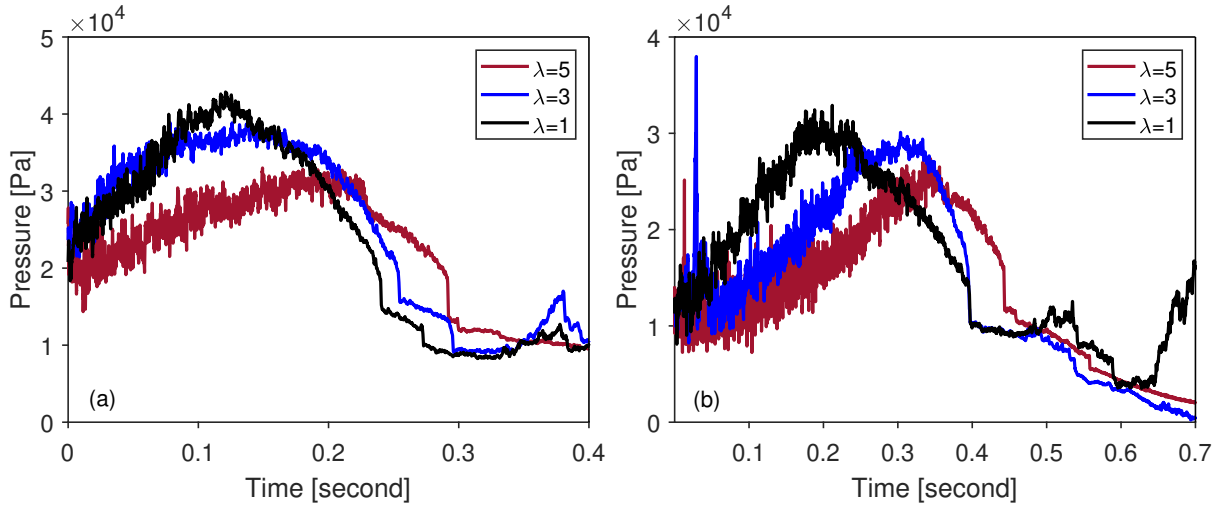

Figure 9: Time evolution of pressure drop along the domains for realizations with different correlation lengths at a) Ca=10^{-5}, and b) Ca=10^{-6}.

invading phase network (green arrows in Fig. 10). These non-local ("distal", as termed by Andrew et al. (2015)) snap-offs can result in immobile or mobile ganglia. As the broken-up finger attempts to attain equilibrium, it starts propagating again within the domain, either to coalesce with the disconnected region or bypass it. For both injection rates (Ca=10^{-5}, 10^{-6}), while interface receding still occurs for λ=5, distal snap-off does not take place. The absence of such pore-level events may be related to the underlying porous microstructure, as follows: the higher correlation length increases the likelihood of larger throats residing next to each other. The snap-off threshold depends on the throats' size, with invading phase snap-off occurring in the smallest throats at the highest capillary pressure (Andrew et al., 2014). The pore space morphology at higher correlations λ generates very low capillary snap-off pressure (due to greater throat size) within the preferred pathways of the invading phase that may hardly be reached. Forcing the non-wetting phase to smaller throats at higher injection rates increases the maximum value of snap-off capillary threshold and raises the chance of non-wet phase break-up as shown in Fig 9 for λ=3. These findings show the influence of correlations on the distal snap-off occurrence. We hypothesize that increasing correlation length reduces the local instabilities of menisci, and enhances the stability of the fluid-fluid interface. This aligns with the observation of Wu et al. (2021) on the greater local instability of interface evolving in domains with more local disorder (corresponding to the lower correlation length in the present study).

Different criteria can be used to indicate the establishment of steady-state conditions. Examples include vanishing variations in the saturation of invading phase (Leclaire et al., 2017) or in interfaces position (Karadimitriou et al., 2016). From the analysis of numerical simulations, we find that for low correlation length (more random disorder), fully stable interface boundaries may not be achievable due to drainage dynamics associated with the disorder. Our analysis indicates that even a minute perturbation caused by a local pore-scale event during the macroscopically steady-state regime, can cause an evident change in interface morphology. To exemplify this, Fig. 11 illustrates the evolution of pressure and saturation for a domain with λ=1 and corresponding fluid configuration at two different times with similar displacement patterns but varying by a single pore invasion. While the saturation of the invading phase reaches a plateau, marginal fluctuation in the pressure gradient can affect the topology of the invading phase causing a snap-off (highlighted with red circles in Fig. 11c,d). Such variations in displacement pattern (e.g. snap-off event) can

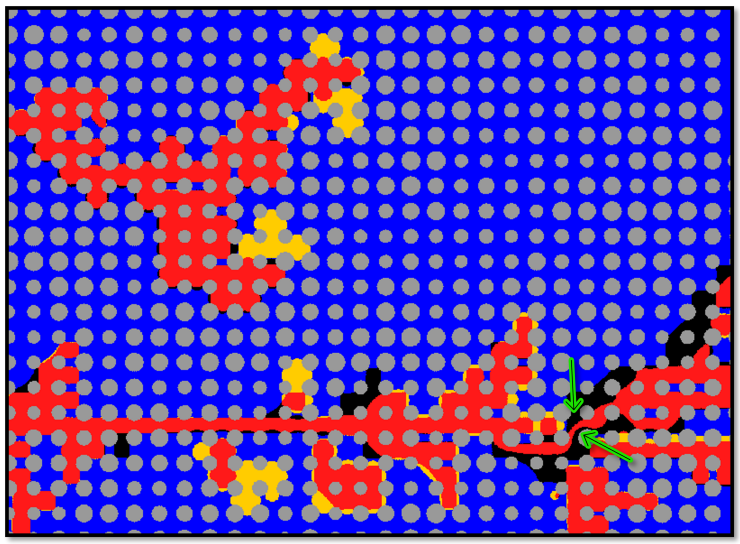

Figure 10: Comparison between multiphase boundaries for a domain with λ=1 at t=t_1, and t=t_2 by superimposing on the same image. Blue and red colour shows the invading and defending phases, respectively. Black areas display interface receding from t_1 to t_2 for invading phase. Yellow areas represent invading phase advancement from t_1 to t_2. Green arrows show interface destabilization within an established finger.

occur repeatedly with further finger thinning and advancement in other locations, according to the pore space characteristics and snap-off pressure. Based on the considered criteria for multiphase steady-state conditions (i.e. marginal variation in saturation or fluids distribution), each of the fluid configurations (Fig. 11c and d) can serve as the steady-state displacement pattern for one-way examining of unsaturated transport. However, the probability distribution of pore-level Pe in Fig. 11b reveals that the transport behavior, at an identical injection rate, varies among the two patterns. The breakup (by snap-off) of a finger which reaches the outlet can alter the streamlines and thus the distribution of flowing-trapped clusters. This rearrangement in velocity pathways evidently affects the spreading and mixing properties of solute particles. In this study, to minimize the effects of alterations in fluid pathways in domains with high local disorder, the quantities (e.g. in dispersion-saturation relation) are determined by averaging them from all realizations and cases with the least rearrangement in fluid-fluid boundaries are mainly considered for analysis.

Interfacial redistribution at steady-state is also a common observation in intermittent flows (i.e. during co-injection of the two phases) (Armstrong et al., 2016; Spurin et al., 2019, 2020). The continuous alteration in fluid connectivity causes the phases to move within porous media through periodic events of disconnection and coalescence. A common approach to study solute transport at this so-called "dynamic steady-state" conditions is to select a fluid arrangement when the saturation of the wetting phase in the domain is nearly constant with minimum variation in fluid pathways (Jimenez-Martinez et al., 2015, 2017). We note, however, that at a constant saturation, interfaces can evolve affecting relative permeability (Armstrong et al., 2016). Given the high sensitivity of transport to the connectivity of pathways (e.g. shown in Fig. 11b for a single snap-off), a more complex transport behavior is expected for intermittent flows compared to the drainage case.

4. Conclusion

The transport of solutes in partially-saturated (two-phase) conditions was studied for porous media with correlated disorder. DNS was used to demonstrate that correlation length in pore sizes

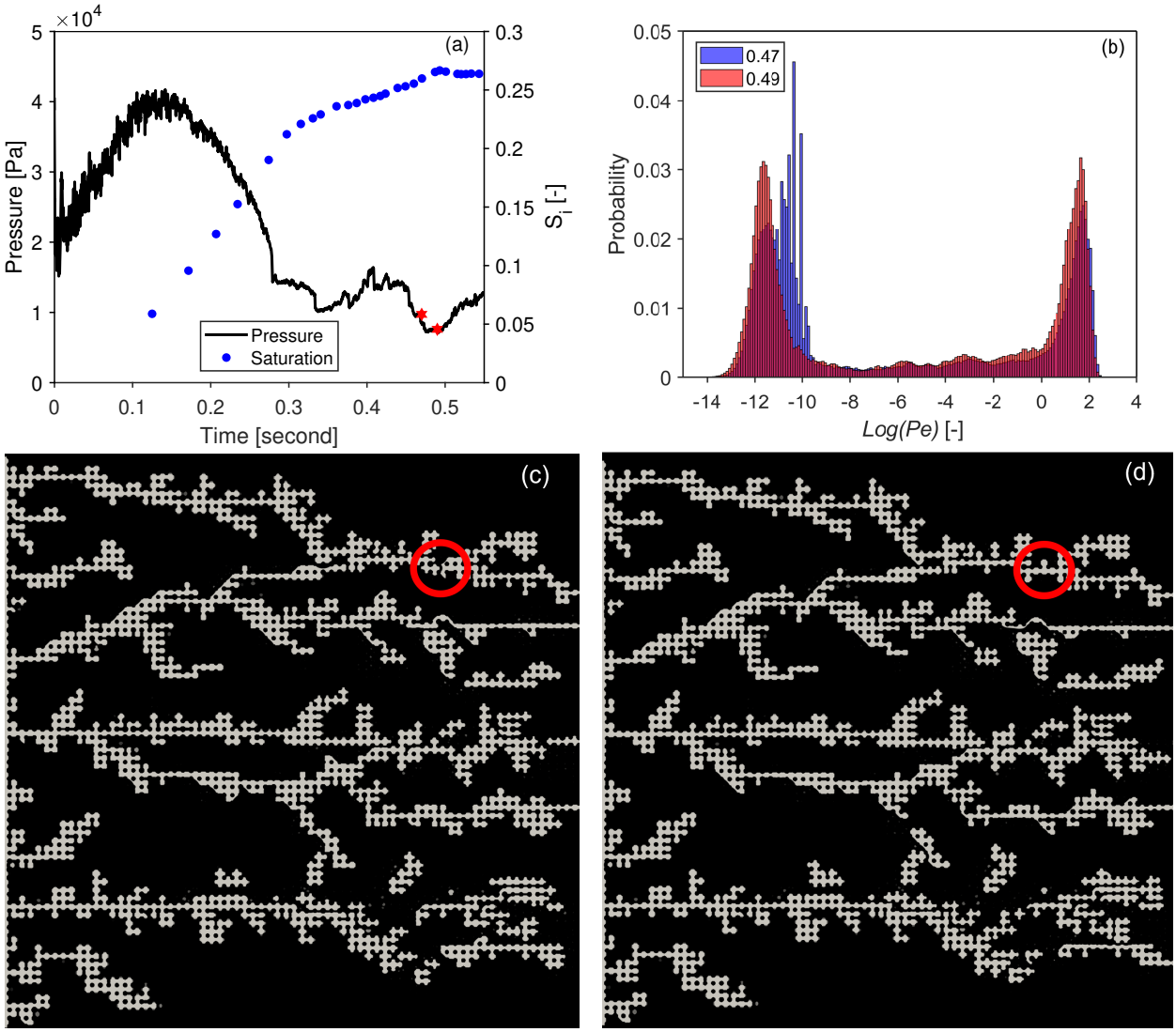

Figure 11: Effect of drainage dynamics on fingering topology for a medium with λ=1 at Ca=10^{-5}, showing: evolution of pressure and saturation with time (a); probability distribution of pore-scale Pe for two adjacent times [shown in red stars in (a), 0.47 (c) and 0.49 second (d)]; and the corresponding invading fluid patterns at 0.47 (c) and 0.49 second (d). The two times are primarily separated by break-up and reconnection in a single pore (red circles in c, d).

can significantly impact the REV of the system (requiring a larger domain), and, consequently, derivation of upscaled quantities. We find that the dispersion coefficient depends on the structural disorder, with a non-monotonic dependence on the invading phase saturation. The presence of fluid-fluid interfaces in the unsaturated case result in bimodal velocity distribution, promoting rapid development of mobile regions and a prolonged diffusive mass flux between mobile and immobile zones. The synergistic effect of advective forces and the arrangement of mobile-immobile clusters influence the magnitude and temporal variation of the diffusive mass flux over time.

Pore-scale disorder is known to have a decisive role on drainage dynamics. This paper demonstrates that increasing the correlation length enhances fluid-fluid interface stability, i.e. time-independent distribution of fluids. We show that even a minor perturbation in invaded phase connectivity, for instance a snap-off in a single pore, can have an evident impact on solute transport by changing the distribution of mobile and immobile zones.

Acknowledgments

The authors acknowledge resources and support from the Scientific Computing Research Technology Platform (SCRTP) at the University of Warwick, and the Faculty of Engineering, Environment and Computing HPC facility at Coventry University. RH acknowledges support from the Engineering and Physical Sciences Research Council (EP/V050613/1).

References

Akai, T., Blunt, M.J., Bijeljic, B., 2020. Pore-scale numerical simulation of low salinity water flooding using the lattice boltzmann method. J. Colloid Interface Sci. 566, 444–453. doi:10.1016/j.jcis.2020.01.065.

Ambekar, A.S., Mattey, P., Buwa, V.V., 2021a. Pore-resolved two-phase flow in a pseudo-3d porous medium: Measurements and volume-of-fluid simulations. Chem. Eng. Sci. 230, 116128.

Ambekar, A.S., Mondal, S., Buwa, V.V., 2021b. Pore-resolved volume-of-fluid simulations of two-phase flow in porous media: Pore-scale flow mechanisms and regime map. Phys. Fluids 33.

An, S., Erfani, H., Godinez-Brizuela, O.E., Niasar, V., 2020a. Transition from viscous fingering to capillary fingering: Application of gpu-based fully implicit dynamic pore network modeling. Water Resour. Res. 56, e2020WR028149. doi:10.1029/2020WR028149.

An, S., Hasan, S., Erfani, H., Babaei, M., Niasar, V., 2020b. Unravelling effects of the pore-size correlation length on the two-phase flow and solute transport properties: Gpu-based pore-network modeling. Water Resour. Res. 56, e2020WR027403. doi:10.1029/2020WR027403.

Andrew, M., Bijeljic, B., Blunt, M.J., 2014. Pore-by-pore capillary pressure measurements using x-ray microtomography at reservoir conditions: Curvature, snap-off, and remobilization of residual co 2. Water Resour. Res. 50, 8760–8774.

Andrew, M., Menke, H., Blunt, M.J., Bijeljic, B., 2015. The imaging of dynamic multiphase fluid flow using synchrotron-based x-ray microtomography at reservoir conditions. Transp. Porous Media 110, 1–24.

Armstrong, R.T., Berg, S., 2013. Interfacial velocities and capillary pressure gradients during haines jumps. Phys. Rev. E 88, 043010.

Armstrong, R.T., McClure, J.E., Berrill, M.A., Rücker, M., Schlüter, S., Berg, S., 2016. Beyond darcy's law: The role of phase topology and ganglion dynamics for two-fluid flow. Phys. Rev. E 94, 043113.

Armstrong, R.T., Sun, C., Mostaghimi, P., Berg, S., Rücker, M., Luckham, P., Georgiadis, A., McClure, J.E., 2021. Multiscale characterization of wettability in porous media. Transp. Porous Media 140, 215–240. doi:10.1007/s11242-021-01615-0.

Aziz, R., Joekar-Niasar, V., Martinez-Ferrer, P., 2018. Pore-scale insights into transport and mixing in steady-state two-phase flow in porous media. Int. J. Multiph. Flow 109, 51–62.

Aziz, R., Joekar-Niasar, V., Martinez-Ferrer, P.J., Godinez-Brizuela, O.E., Theodoropoulos, C., Mahani, H., 2019. Novel insights into pore-scale dynamics of wettability alteration during low salinity waterflooding. Sci. Rep. 9, 1–13.

Babaei, M., Joekar-Niasar, V., 2016. A transport phase diagram for pore-level correlated porous media. Adv. Water Resour. 92, 23–29.

Ben-Noah, I., Hidalgo, J.J., Jimenez-Martinez, J., Dentz, M., 2023. Solute trapping and the mechanisms of non-fickian transport in partially saturated porous media. Water Resour. Res. 59, e2022WR033613.

Biswas, S., Fantinel, P., Borgman, O., Holtzman, R., Goehring, L., 2018. Drying and percolation in correlated porous media. Phys. Rev. Fluids 3, 124307. doi:10.1103/PhysRevFluids.3.124307.

Blunt, M.J., 2017. Multiphase Flow in Permeable Media: A Pore-Scale Perspective. Cambridge University Press, Cambridge. doi:10.1017/9781316145098.

Borgman, O., Darwent, T., Segre, E., Goehring, L., Holtzman, R., 2019. Immiscible fluid displacement in porous media with spatially correlated particle sizes. Adv. Water Resour. 128, 158–167. doi:10.1016/j.advwatres.2019.04.015.

Borgman, O., Fantinel, P., Lühder, W., Goehring, L., Holtzman, R., 2017. Impact of spatially correlated pore-scale heterogeneity on drying porous media. Water Resour. Res. 53, 5645–5658.

Borgman, O., Turuban, R., Géraud, B., Le Borgne, T., Méheust, Y., 2023. Solute front shear and coalescence control concentration gradient dynamics in porous micromodel. Geophys. Res. Lett. 50, e2022GL101407.

Brackbill, J.U., Kothe, D.B., Zemach, C., 1992. A continuum method for modeling surface tension. Journal of Computational Physics 100, 335–354. doi:10.1016/0021-9991(92)90240-Y.

Chang, C., Kneafsey, T.J., Zhou, Q., Oostrom, M., Ju, Y., 2019. Scaling the impacts of pore-scale characteristics on unstable supercritical co2-water drainage using a complete capillary number. Int. J. Greenh. Gas Control 86, 11–21.

Cussler, E.L., 2009. Diffusion: mass transfer in fluid systems. Cambridge university press.

Dashtian, H., Shokri, N., Sahimi, M., 2018. Pore-network model of evaporation-induced salt precipitation in porous media: The effect of correlations and heterogeneity. Adv. Water Resour. 112, 59–71.

Erfani, H., Karadimitriou, N., Nissan, A., Walczak, M.S., An, S., Berkowitz, B., Niasar, V., 2021. Process-dependent solute transp. porous media. Transp. Porous Media 140, 421–435.

Ferrari, A., Lunati, I., 2013. Direct numerical simulations of interface dynamics to link capillary pressure and total surface energy. Adv. Water Resour. 57, 19–31.

Gong, Y., Piri, M., 2020. Pore-to-core upscaling of solute transport under steady-state two-phase flow conditions using dynamic pore network modeling approach. Transp. Porous Media 135, 181–218.

Guédon, G.R., Inzoli, F., Riva, M., Guadagnini, A., 2019. Pore-scale velocities in three-dimensional porous materials with trapped immiscible fluid. Phys. Rev. E 100, 043101.

Guillon, V., Fleury, M., Bauer, D., Neel, M.C., 2013. Superdispersion in homogeneous unsaturated porous media using nmr propagators. Phys. Rev. E 87, 043007.

Hammel, K., Roth, K., 1998. Approximation of asymptotic dispersivity of conservative solute in unsaturated heterogeneous media with steady state flow. Water Resour. Res. 34, 709–715.

Hasan, S., Joekar-Niasar, V., Karadimitriou, N.K., Sahimi, M., 2019. Saturation dependence of non-fickian transp. porous media. Water Resour. Res. 55, 1153–1166.

Holtzman, R., 2016. Effects of pore-scale disorder on fluid displacement in partially-wettable porous media. Sci. Rep. 6, 36221. doi:10.1038/srep36221.

Holtzman, R., Segre, E., 2015. Wettability stabilizes fluid invasion into porous media via nonlocal, cooperative pore filling. Phys. Rev. Lett. 115, 164501.

Issa, R.I., 1986. Solution of the implicitly discretised fluid flow equations by operator-splitting. J. Comput. Phys. 62, 40–65.

Jimenez-Martinez, J., Alcolea, A., Straubhaar, J.A., Renard, P., 2020. Impact of phases distribution on mixing and reactions in unsaturated porous media. Adv. Water Resour. 144, 103697.

Jimenez-Martinez, J., Anna, P.d., Tabuteau, H., Turuban, R., Borgne, T.L., Meheust, Y., 2015. Pore-scale mechanisms for the enhancement of mixing in unsaturated porous media and implications for chemical reactions. Geophys. Res. Lett. 42, 5316–5324.

Jimenez-Martinez, J., Le Borgne, T., Tabuteau, H., Meheust, Y., 2017. Impact of saturation on dispersion and mixing in porous media: Photobleaching pulse injection experiments and shear-enhanced mixing model. Water Resour. Res. 53, 1457–1472.

Kapetas, L., Dror, I., Berkowitz, B., 2014. Evidence of preferential path formation and path memory effect during successive infiltration and drainage cycles in uniform sand columns. J. Contam. Hydrol. 165, 1–10.

Karadimitriou, N.K., Joekar-Niasar, V., Babaei, M., Shore, C.A., 2016. Critical role of the immobile zone in non-fickian two-phase transport: A new paradigm. Environ. Sci. Technol. 50, 4384–4392.

Karadimitriou, N.K., Joekar-Niasar, V., Brizuela, O.G., 2017. Hydro-dynamic solute transport under two-phase flow conditions. Sci. Rep. 7, 1–7.

Khayrat, K., Jenny, P., 2016. Subphase approach to model hysteretic two-phase flow in porous media. Transp. Porous Media 111, 1–25.

Larsen, B.E., Fuhrman, D.R., Roenby, J., 2019. Performance of interfoam on the simulation of progressive waves. Coast. Eng. J. 61, 380–400.

Leclaire, S., Parmigiani, A., Malaspinas, O., Chopard, B., Latt, J., 2017. Generalized three-dimensional lattice boltzmann color-gradient method for immiscible two-phase pore-scale imbibition and drainage in porous media. Phys. Rev. E 95, 033306.

Li, P., Berkowitz, B., 2019. Characterization of mixing and reaction between chemical species during cycles of drainage and imbibition in porous media. Adv. Water Resour. 130, 113–128.

Mehmani, A., Verma, R., Prodanović, M., 2020. Pore-scale modeling of carbonates. Mar. Pet. Geol. 114, 104141.

Mehmani, Y., Balhoff, M.T., 2015. Mesoscale and hybrid models of fluid flow and solute transport. Rev. Mineral. Geochem. 80, 433–459.

Mehmani, Y., Oostrom, M., Balhoff, M.T., 2014. A streamline splitting pore-network approach for computationally inexpensive and accurate simulation of transp. porous media. Water Resour. Res. 50, 2488–2517.

Mehmani, Y., Tchelepi, H.A., 2017. Minimum requirements for predictive pore-network modeling of solute transport in micromodels. Adv. Water Resour. 108, 83–98.

Moebius, F., Or, D., 2012. Interfacial jumps and pressure bursts during fluid displacement in interacting irregular capillaries. J. Colloid Interface Sci. 377, 406–415. doi:doi.org/10.1016/j.jcis.2012.03.070.

Moreno-Atanasio, R., Williams, R.A., Jia, X., 2010. Combining x-ray microtomography with computer simulation for analysis of granular and porous materials. Particuology 8, 81–99.

Moukalled, F., Mangani, L., Darwish, M., 2016. The finite volume method in computational fluid dynamics. volume 113. Springer.

Moura, M., Måløy, K.J., Flekkøy, E.G., Toussaint, R., 2020. Intermittent dynamics of slow drainage experiments in porous media: Characterization under different boundary conditions. Front. Phys. 7, 217.

Neuman, S.P., Tartakovsky, D.M., 2009. Perspective on theories of non-fickian transport in heterogeneous media. Adv. Water Resour. 32, 670–680.

Nordahl, K., Ringrose, P.S., 2008. Identifying the representative elementary volume for permeability in heterolithic deposits using numerical rock models. Math. Geosci. 40, 753–771.

Noughabi, R.S., Mansouri, S.H., Raoof, A., 2023. Interface-induced dispersion in the unsaturated porous media: a pore-scale perspective. Adv. Water Resour. , 104474.

Nützmann, G., Maciejewski, S., Joswig, K., 2002. Estimation of water saturation dependence of dispersion in unsaturated porous media: experiments and modelling analysis. Adv. Water Resour. 25, 565–576.

Ogata, A., Banks, R.B., 1961. A solution of the differential equation of longitudinal dispersion in porous media. US Government Printing Office.

Persson, B.N., Albohr, O., Tartaglino, U., Volokitin, A., Tosatti, E., 2004. On the nature of surface roughness with application to contact mechanics, sealing, rubber friction and adhesion. J. Condens. Matter Phys. 17, R1.

Rabbani, H.S., Joekar-Niasar, V., Shokri, N., 2016. Effects of intermediate wettability on entry capillary pressure in angular pores. J. Colloid Interface Sci. 473, 34–43. doi:https://doi.org/10.1016/j.jcis.2016.03.053.

Rabbani, H.S., Or, D., Liu, Y., Lai, C.Y., Lu, N.B., Datta, S.S., Stone, H.A., Shokri, N., 2018. Suppressing viscous fingering in structured porous media. Proc. Natl. Acad. Sci. 115, 4833–4838. doi:10.1073/pnas.1800729115.

Raeini, A.Q., Bijeljic, B., Blunt, M.J., 2014. Numerical modelling of sub-pore scale events in two-phase flow through porous media. Transp. Porous Media 101, 191–213.

Raoof, A., Hassanizadeh, S., 2013. Saturation-dependent solute dispersivity in porous media: pore-scale processes. Water Resour. Res. 49, 1943–1951.

Raoof, A., Nick, H.M., Hassanizadeh, S.M., Spiers, C., 2013. Poreflow: A complex pore-network model for simulation of reactive transport in variably saturated porous media. Comput. Geosci. 61, 160–174.

Reynolds, C.A., Menke, H., Andrew, M., Blunt, M.J., Krevor, S., 2017. Dynamic fluid connectivity during steady-state multiphase flow in a sandstone. Proc. Natl. Acad. Sci. 114, 8187–8192.

Roman, S., Soulaine, C., Kovscek, A.R., 2020. Pore-scale visualization and characterization of viscous dissipation in porous media. J. Colloid Interface Sci. 558, 269–279.

Saeibehrouzi, A., Abolfathi, S., Denissenko, P., Holtzman, R., 2024. Pore-scale modeling of solute transport in partially-saturated porous media doi:10.22541/au.170709025.51643762/v1.

Sahimi, M., 2012. Dispersion in porous media, continuous-time random walks, and percolation. Phys. Rev. E 85, 016316.

Sato, T., Tanahashi, H., Loáiciga, H.A., 2003. Solute dispersion in a variably saturated sand. Water Resour. Res. 39.

Scanziani, A., Singh, K., Blunt, M.J., Guadagnini, A., 2017. Automatic method for estimation of in situ effective contact angle from x-ray micro tomography images of two-phase flow in porous media. J. Colloid Interface Sci. 496, 51–59.

Scheibe, T.D., Murphy, E.M., Chen, X., Rice, A.K., Carroll, K.C., Palmer, B.J., Tartakovsky, A.M., Battiato, I., Wood, B.D., 2015. An analysis platform for multiscale hydrogeologic modeling with emphasis on hybrid multiscale methods. Groundwater 53, 38–56.

Schlüter, S., Vanderborght, J., Vogel, H.J., 2012. Hydraulic non-equilibrium during infiltration induced by structural connectivity. Adv. Water Resour. 44, 101–112.

Shende, T., Niasar, V., Babaei, M., 2021. Pore-scale simulation of viscous instability for non-newtonian two-phase flow in porous media. J. Non-newton. Fluid Mech. 296, 104628.

Spurin, C., Bultreys, T., Bijeljic, B., Blunt, M.J., Krevor, S., 2019. Intermittent fluid connectivity during two-phase flow in a heterogeneous carbonate rock. Phys. Rev. E 100, 043103.

Spurin, C., Bultreys, T., Rücker, M., Garfi, G., Schlepütz, C.M., Novak, V., Berg, S., Blunt, M.J., Krevor, S., 2020. Real-time imaging reveals distinct pore-scale dynamics during transient and equilibrium subsurface multiphase flow. Water Resour. Res. 56, e2020WR028287.

Spurin, C., Bultreys, T., Rücker, M., Garfi, G., Schlepütz, C.M., Novak, V., Berg, S., Blunt, M.J., Krevor, S., 2021. The development of intermittent multiphase fluid flow pathways through a porous rock. Adv. Water Resour. 150, 103868. doi:10.1016/j.advwatres.2021.103868.

Suo, S., Liu, M., Gan, Y., 2020. Fingering patterns in hierarchical porous media. Phys. Rev. Fluids 5, 034301.

Tahmasebi, P., Kamrava, S., 2018. Rapid multiscale modeling of flow in porous media. Phys. Rev. E 98, 052901.

Timms, W.A., Acworth, R.I., Crane, R.A., Arns, C.H., Arns, J.Y., McGeeney, D.E., Rau, G.C., Cuthbert, M.O., 2018. The influence of syndepositional macropores on the hydraulic integrity of thick alluvial clay aquitards. Water Resour. Res. 54, 3122–3138.

Triadis, D., Jiang, F., Bolster, D., 2019. Anomalous dispersion in pore-scale simulations of two-phase flow. Transp. Porous Media 126, 337–353.

Ursino, N., Gimmi, T., Flühler, H., 2001. Dilution of non-reactive tracers in variably saturated sandy structures. Advances in water resources 24, 877–885.

Van Genuchten, M.T., Wierenga, P., 1976. Mass transfer studies in sorbing porous media i. analytical solutions. Soil Sci. Soc. Am. J. 40, 473–480.

Vanderborght, J., Vereecken, H., 2007. Review of dispersivities for transport modeling in soils. Vadose Zone J. 6, 29–52.

Vik, B., Bastesen, E., Skauge, A., 2013a. Evaluation of representative elementary volume for a vuggy carbonate rock—part: Porosity, permeability, and dispersivity. J. Pet. Sci. Eng. 112, 36–47. doi:10.1016/j.petrol.2013.03.029.

Vik, B., Sylta, K., Skauge, A., 2013b. Evaluation of representative elementary volume for a vuggy carbonate rock–part ii: Two-phase flow. J. Pet. Sci. Eng. 112, 48–60.

Wang, Z., Pereira, J.M., Gan, Y., 2021. Effect of grain shape on quasi-static fluid-fluid displacement in porous media. Water Resour. Res. 57, e2020WR029415.

Wei, H., Zhu, X., Liu, X., Yang, H., Tao, W.Q., Chen, L., 2022. Pore-scale study of drainage processes in porous media with various structural heterogeneity. Int. Commun. Heat Mass Transf. 132, 105914.

Wu, D.S., Hu, R., Lan, T., Chen, Y.F., 2021. Role of pore-scale disorder in fluid displacement: Experiments and theoretical model. Water Resour. Res. 57, e2020WR028004.

Yang, Y., Cai, S., Yao, J., Zhong, J., Zhang, K., Song, W., Zhang, L., Sun, H., Lisitsa, V., 2021. Pore-scale simulation of remaining oil distribution in 3d porous media affected by wettability and capillarity based on volume of fluid method. Int. J. Multiph. Flow 143, 103746.

Young, T., 1805. Iii. an essay on the cohesion of fluids. Philosophical transactions of the royal society of London , 65–87.

Zhang, C., Oostrom, M., Wietsma, T.W., Grate, J.W., Warner, M.G., 2011. Influence of viscous and capillary forces on immiscible fluid displacement: Pore-scale experimental study in a water-wet micromodel demonstrating viscous and capillary fingering. Energy Fuels 25, 3493–3505.

Zhuang, L., Raoof, A., Mahmoodlu, M.G., Biekart, S., de Witte, R., Badi, L., van Genuchten, M.T., Lin, K., 2021. Unsaturated flow effects on solute transp. porous media. J. Hydrol. 598, 126301.